Real-time observation of hydrogen absorption by $LaNi_5$ with quasi-dynamic neutron tomography

Citation	Wood, B. M., Ham, K., Hussey, D. S., Jacobson, D. L., Faridani, A., Kaestner, A., ... & Butler, L. G. (2014). Real-time observation of hydrogen absorption by $LaNi_5$ with quasi-dynamic neutron tomography. Nuclear Instruments and Methods in Physics Research Section B: Beam Interactions with Materials and Atoms, 324, 95-101. doi:10.1016/j.nimb.2013.10.052
DOI	10.1016/j.nimb.2013.10.052
Publisher	Elsevier
Version	Version of Record
Citable Link	http://hdl.handle.net/1957/48224
Terms of Use	http://cdss.library.oregonstate.edu/sa-termsofuse

Nuclear Instruments and Methods in Physics Research B 324 (2014) 95–101

Contents lists available at ScienceDirect

Nuclear Instruments and Methods in Physics Research B

journal homepage: www.elsevier.com/locate/nimb

Real-time observation of hydrogen absorption by $LaNi_5$ with quasi-dynamic neutron tomography

Bradley M. Wood [b], Kyungmin Ham [a], Daniel S. Hussey [c], David L. Jacobson [c], Adel Faridani [d], Anders Kaestner [e], John J. Vajo [f], Ping Liu [f], Tabbetha A. Dobbins [g], Leslie G. Butler [b,*]

[a] Center for Advanced Microstructures and Devices, Louisiana State University, Baton Rouge, LA 70806, USA
[b] Department of Chemistry, Louisiana State University, Baton Rouge, LA 70803, USA
[c] Neutron Imaging Group, National Institute of Standards and Technology, 100 Bureau Dr., Mail Stop 8461, Gaithersburg, MD 20899-8461, USA
[d] Department of Mathematics, Oregon State University, Corvallis, OR 97331, USA
[e] Paul Scherrer Institut, Neutron Imaging and Activation Group, CH-5232 Villigen, Switzerland
[f] HRL Labs LLC, Malibu, CA 90265, USA
[g] Department of Physics & Astronomy, Rowan University, Glassboro, NJ 08028-1701, USA

ARTICLE INFO

Article history:
Received 16 July 2013
Received in revised form 20 August 2013
Accepted 23 October 2013
Available online 18 January 2014

Keywords:
Neutron tomography
Dynamic tomography
Hydrogen storage

ABSTRACT

The uptake of hydrogen by lanthanum pentanickel ($LaNi_5$) to form lanthanum nickel hydride ($LaNi_5H_6$) is followed with three-dimensional imaging by neutron tomography. The hydrogen absorption process is slower than the time needed for acquiring a single radiograph, about 10 s, but fast relative to the time to acquire a fully-sampled tomographic data set, about 6000 s. A novel data acquisition scheme is used with angles based upon the Greek Golden ratio, a scheme which allows considerable flexibility in post-acquisition tomography reconstruction. Even with tomographic undersampling, the granular structure for the conversion of $LaNi_5$ particles to $LaNi_5H_6$ particles is observed and visually tracked in 3D. Over the course of five sequential hydrogen uptake runs with various initial hydrogen pressures, some grains are repeatedly observed.

1. Introduction

Stop-action photography has been widely used to probe many phenomena, such as the stride of a galloping horse [1]. Now let us imagine the power of 3D stop-action imaging of chemical processes inside high-pressure, metal-wall reaction vessels. Neutron tomography provides a view into the reaction vessel; the Greek Golden ratio gives post-acquisition data processing freedom as the tomography raw data is converted into sequential 3D data sets.

The absorption of hydrogen by metal alloys is an ideal process for neutron imaging as neutrons easily penetrate most metals, yet are strongly attenuated by the ^1H isotope [2,3]. Sakaguchi and co-workers imaged ingots of Mg–Ni alloys after reaction with aqueous sodium borohydride solution; 2D and 3D images of the dried ingots show the hydrogen absorption depth increasing with reaction time [4]. In a larger sample, ^2H isotope was imaged as portions of the cryocooler before and after $^2H_2$ absorption [5,6].

The study of chemical kinetics is one of the more exacting tasks in the laboratory. For the hydrogen uptake/desorption reaction, the task is even more daunting because of the drastic changes in morphology upon hydrogenation-including volume expansion and particle fracture. Tomographic 3D imaging is extremely useful for tracking such changes associated with hydrogenation/dehydrogenation.

Herein, we describe a data acquisition procedure based upon the Greek Golden ratio that reduces the overall timescale for data collection at the beamline. Rather, this time is transferred to the post-acquisition phase of the experiment in which trial tomographic reconstructions are performed in a search for an optimum balance of time resolution with acceptable image signal-to-noise ratio. Kaestner et al. have analyzed the Greek Golden ratio and a related binary decomposition scheme; both schemes are proposed for aiding time-resolved tomography imaging [7]. The Greek Golden ratio scheme was used to follow a battery discharge process [8]. This work uses it to track *in situ* hydrogenation of $LaNi_5$, while exploring the projection time scale windows.

2. Theory

In tomography, the data acquisition portion of the experiment is dominated by accurately acquiring a series of N_p-projections that

* Corresponding author.
E-mail addresses: bwood6@tigers.lsu.edu (B.M. Wood), kham1@lsu.edu (K. Ham), daniel.hussey@nist.gov (D.S. Hussey), david.jacobson@nist.gov (D.L. Jacobson), faridani@science.oregonstate.edu (A. Faridani), anders.kaestner@psi.ch (A. Kaestner), JJVajo@hrl.com (J.J. Vajo), PLiu@hrl.com (P. Liu), Dobbins@rowan.edu (T.A. Dobbins), lbutler@lsu.edu (L.G. Butler).

0168-583X/$ - see front matter © 2014 Elsevier B.V. All rights reserved.
http://dx.doi.org/10.1016/j.nimb.2013.10.052

measure the attenuation of N_u-equally-spaced parallel rays through the sample. The total number of projections needed to define the entire reconstructed image is $N_p = \frac{\pi}{2} N_u$ [9], though in practice, many users often under-sample in a tradeoff between total acquisition time and spatial resolution of a portion of reconstructed image. For reasons offering minor experimental conveniences, the common practice has been to use projection angles ordered by a simple, fixed angle increment:

$$\begin{aligned} \theta \text{ (fixed angle)} &= \{0, \Delta\theta, 2\Delta\theta, 3\Delta\theta, \ldots \pi - (N_p - 1)\Delta\theta\} \\ \text{where } \Delta\theta &= \tfrac{\pi}{N_p} \end{aligned} \tag{1}$$

This time-ordering of the projection angles has minimal sample motion and a modest programming advantage; the projection image files have extension numbers that monotonically map onto the projection angle list. The problem with projection angles based on fixed angle increments is that it leads to an all-or-nothing data acquisition strategy. If, say, the last 10% of the required angles are missed, then the reconstruction—here, we are assuming a filtered back-projection reconstruction—is compromised by the missing data, yielding significant artifacts in the tomographic image.

Köhler [10] cleverly recognized projection acquisition as an exercise in convergence and was also inspired by the way some plants position their leaves, with the angle between successive leaves on a stem of approximately $\pi g \approx 222^\circ$ where $g = \frac{\sqrt{5}+1}{2} \approx 1.61803$, the Greek Golden ratio [11]. Köhler proposed, mainly for the purpose of reducing radiation exposure for patients in CT tomography, a projection angle sequence of

$$\begin{aligned} \theta \text{ (Greek golden)} &= \big[\{0, g, 2g, \ldots, (N_p - 1)g\} k\pi, \ldots \\ &\quad \textbf{mod } k\pi\big] \end{aligned} \tag{2}$$

where $k = 1$ for scans of $[0, \pi)$ and $k = 2$ for scans of $[0, 2\pi)$ and again, the tomographer can elect to under-sample. However, now under-sampling can be freely invoked during post-acquisition processing at any point in the angle list, offering remarkable freedom in the tomography experiment. In addition, the angle list can be started at an arbitrary angle. The angular spacing between projections is variable; the weighting scheme for the q_{th} projection during reconstruction is simply

$$w_j = \frac{(q_{j+1} + q_j) - (q_j + q_{j-1})}{2(k\pi)} \qquad j = [2, N-1] \tag{3}$$

$$w_1 = \frac{(k\pi - q_1) + (q_2 - q_1)}{2(k\pi)} \tag{4}$$

$$w_N = \frac{(k\pi - q_N) + (q_N - q_{N-1})}{2(k\pi)}. \tag{5}$$

Kazantsev and coworkers numerically assessed several projection ordering strategies: the traditional fixed-angle increment, a random angle scheme, a weighted distance schema, and an angle set based upon the Greek Golden ratio [12]. The Greek Golden ratio scheme is, in our experience, easily implemented and offers good performance.

To reduce time spent with a slow rotation stage, several thousand angles were generated using Eq. (2) and then sorted in groups of fifty monotonically ascending, then descending angles, as shown in Fig. 1A.

After the tomography data acquisition finished, time windows were established based upon the total time for an experimental run and the hydrogen uptake; projections from those time windows were selected for tomographic reconstruction. For example, the first 500 projections in run #4 used the angles shown in Fig. 1A. After acquisition, several reconstructions were considered based on the rate of hydrogen absorption and the signal-to-noise ratio of the reconstructed volumes. The selected angle sets for two different reconstructions are shown in Figs. 1B, C and 2A, B. Reconstructions from the former have better

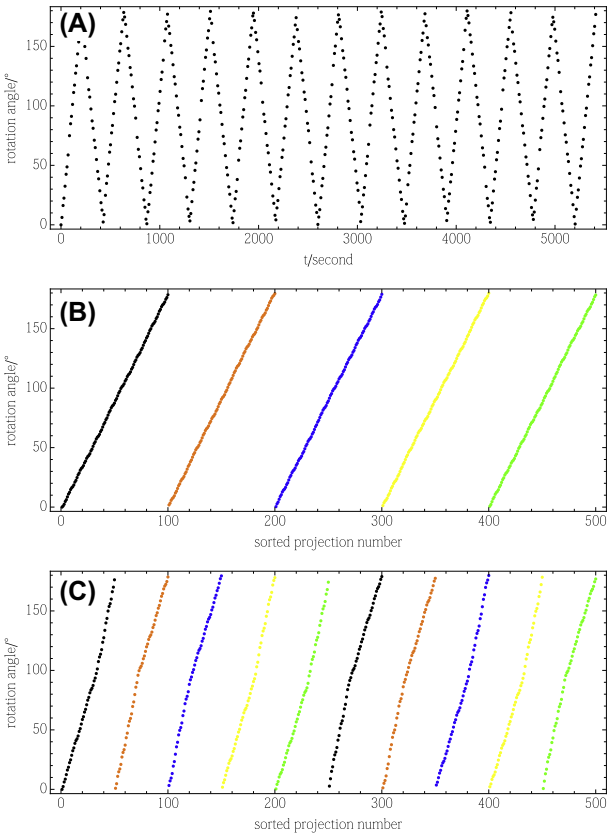

Fig. 1. The tomography sample rotation angles used in run #4 for the first 500 projections. In (A), the angles are ordered by time, while in (B) and (C), the angles are resorted in groups of (B) 100 projections and (C) 50 projections prior to tomographic reconstruction.

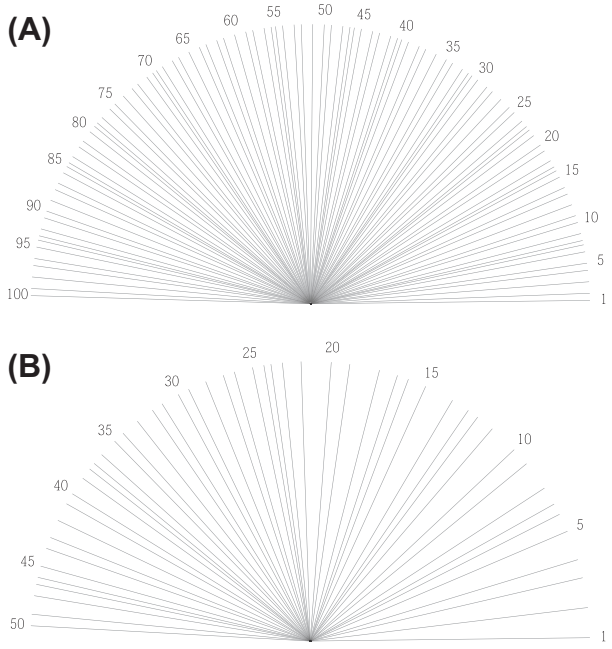

Fig. 2. The fan views show the sorted angles in the last set of (A) 100 and (B) 50 projections, respectively.

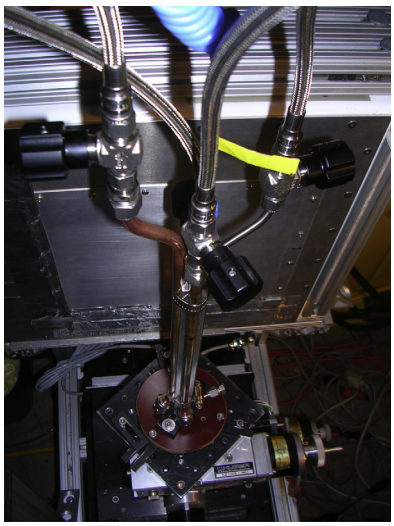

(a) Four tubes of the sample holder clamped to a central aluminum bar and mounted on the rotation stage.

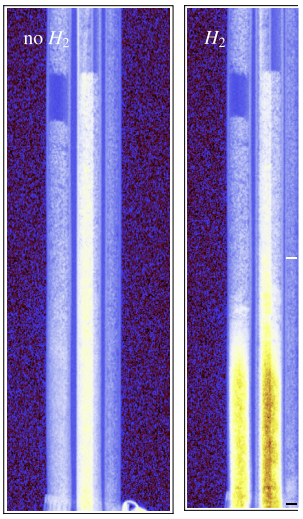

(b) Neutron absorption looking from reactor to the detector for no-H_2 and 28.8% H_2. Field-of-view = 1500x500 pixels.

Fig. 3. (a) Four flexible hoses are connected to two 6.35 mm (1/4″) OD stainless steel and two 9.52 mm (3/8″) OD copper tubing sections, all filled with $LaNi_5$ (not sieved). The tubes are clustered around an aluminum mounting bar and mounted on top of the rotation stage, which is visible at the bottom of the photograph. The flat plate behind the sample is a thin aluminum cover over the scintillator. (b) Transmission neutron radiographs at 0% and 28.8% H_2 saturation of the sample showing the partial activation of $LaNi_5$. In the lower right corner is part of a stainless steel hose clamp used to affix the tubes to the central aluminum bar. These images are 2D projection of the sample and show the filling of hydrogen, indicated by red color in images (right) associated with beam attenuation. The samples chambers were filled with H_2 gas from the bottom.

spatial resolution while the latter angle set has a twofold better time resolution.

The lengths of the sorted lists used in Figs. 1 and 2 were fixed at multiples of ten for procedure development. It is likely that improved performance would be found with lists lengths set to Fibonacci numbers, such as 55, 89 and 144.

In this work, we make no correction for motion that occurs within a time window. That problem has been address by Katsevich with an error term that compensates for motion [13], a procedure which also compensates for errors in the assumed center of rotation [14].

3. Experimental

3.1. Sample and sample holder

Previous neutron imaging [5] of $LaNi_{4.78}Sn_{0.22}$ undergoing absorption of $^2H_2$ had used a cylindrical sample, therefore, a similar sample geometry was used for the present work, though consisting of four parallel tubes. To a first order approximation, estimates of transmission values were calculated from the sum of the neutron scattering and absorption cross sections for thermal neutrons [3] for $LaNi_5$ and $LaNi_5H_6$, yielding $1/e$ path lengths of 6.9 mm and 1.4 mm, respectively. The simple sample holder consisted of lengths of 6.35 mm (1/4″) OD stainless steel and 9.52 mm (3/8″) OD copper tubing mounted to an aluminum mounting bar; gas fittings were Swageloc[1] tubing fittings as shown in Fig. 3a, and connected to the beamline's hydrogen gas manifold with Teflon-lined flexible metal hoses. The aluminum mounting bar was also affixed with small diameter hole for mounting a thermocouple probe and a 6.35 mm (1/4″) threaded rod, secured with a perpendicular set screw, for mounting to the tomography rotation stage. The stainless steel and copper tubes were loaded in air with 113 g of Ergenics HyStor 205 Alloy 12 mesh $LaNi_5$. For the high resolution tomography run, three alumina spheres were used as spacers between sieved ($\geqslant$1.19 mm) grains of $LaNi_5$.

The samples were evacuated to 0.2 Pa with a BOC Edmonds turbomolecular pumping station while heating to 175°C for 1 h, then cooled and charged with H_2. In the first experimental series with an H_2 activation pressure of 1.34 MPa, the sample was activated to only 28.8% as evident in Fig. 3b. In the second experimental series, an H_2 activation pressure of 2.76 MPa yielded complete activation; this sample was used for the results shown in Figs. 5 and 6.

3.2. Hydrogen gas manifold

The sample cell was pressure tested with N_2 to 125% of the maximum permitted working pressure of 2.31 MPa for this sample container. The beamline H_2 gas manifold controls have been in a rapid state of development, but at the time of these experiments, controls existed for slow H_2 addition to the sample, but evacuation could not be slowed sufficiently to enable tomography of H_2 desorption. In the absorption imaging experiments, a reservoir volume of 2.40 L was pressurized with H_2, then slowly released into the manifold and sample, all having a total volume of 3.01 L as measured with N_2 gas experiments. During tomography runs, absolute manifold pressure was logged at 1 min intervals with a resolution of 100 Pa using a Mensur Corporation CPG 2500 digital pressure gauge. The H_2 gas came from two sources: Below

[1] Certain trade names and company products are mentioned in the text or identified in an illustration in order to adequately specify the experimental procedure and equipment used. In no case does such identification imply recommendation or endorsement by NIST, nor does it imply that the products are necessarily the best available for this purpose.

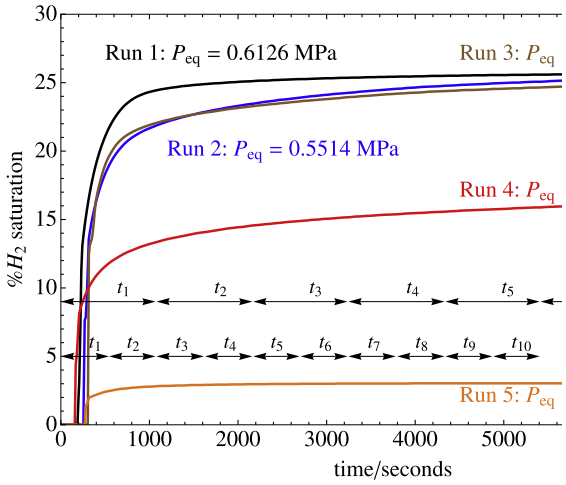

Fig. 4. The H_2 saturation measured from manifold pressure during the course of five tomography runs. Also shown, with double-headed arrows, are the times used to define tomography reconstructions based on the post-acquisition angle selection possible with the Greek Golden ratio angles, as illustrated in Fig. 1.

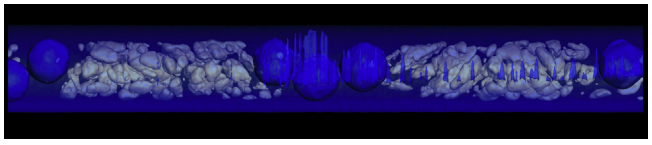

Fig. 5. A cut-away slice of the neutron tomogram of the 4.4 mm ID stainless steel pipe revealing the individual $LaNi_5H_6$ grains under 0.4 MPa H_2. The blue spheres are spacers of Al_2O_3 added to the sample tube; the sample mass between spheres is 1 g, corresponding roughly 10–20 grains (sieved, particle size $\geqslant$1.19 mm) in the initial sample preparation.

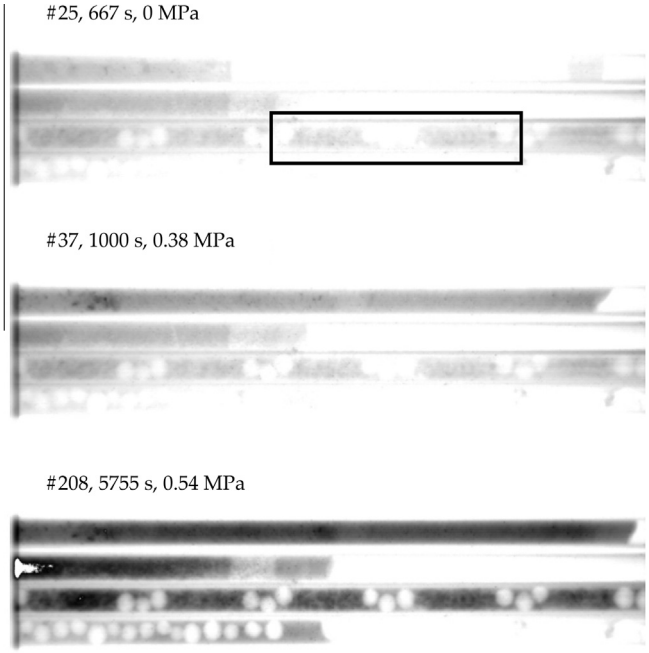

Fig. 6. Three frames from a movie of 2D radiography show H_2 absorption into $LaNi_5$ (sieved) filled stainless steel tubes. The H_2 gas enters from the right. The tube section selected for high resolution tomography (Fig. 5) is outlined by a rectangle and contains $\approx$1 g of $\geqslant$1.19 mm $LaNi_5$ grains between each trio of spherical alumina spacers. The three images are shown on a common grayscale with black corresponding to high neutron attenuation (high hydrogen concentration).

550 kPa, H_2 was generated electrolytically from water. Up to 2.31 MPa, H_2 from a gas cylinder with a Tescom 0–4 MPa psi regulator was used to charge the 2.40 L reservoir; for safety, the gas cylinder main value was closed at all times other than reservoir recharging.

3.3. Beamline neutron optics

The neutron pinhole optics were set to an L/D $\approx$ 600 giving a thermal neutron fluence at the sample position of 4.97×10^6 cm^{-2} s^{-1}. The neutrons were detected with a 0.3 mm thick ^{6}LiF-doped ZnS scintillator screen observed by an amorphous silicon flat panel detector in direct contact with the scintillator. Detector pixel size was 127 μm square; with 1 s acquisition time per projection, this gives on average 780 neutrons incident on each pixel in each projection. A flat field image was taken three times throughout the tomography runs, each consisting of 900 s acquisition, which was then rescaled to an equivalent 1 s projection acquisition; average count over a flat field was 1480 ± 92 counts (one standard deviation); the dark field was 16 ± 6 counts. The detector operated with a 14-bit digitizer. The sample-to-scintillator distance was 12.3 cm giving a geometric blur of 205 μm. The tomography rotation stage was driven by a stepper motor lacking an on-shaft encoder. Observation of the rotation stage dial indicator throughout the runs revealed a small, cumulative error on the order of 1–2° per tomography run. Therefore, during data analysis, prior to any difference image calculations between runs, one volume was rotated based on an angle calculated from control points shared between the two volumes.

In a second experimental run for static, high resolution tomography, the previous rotation stage was upgraded to a Newport URS150BCC stage that was controlled by a rotary encoded DC servo motor that eliminated errors in step angles. The high resolution detector used a 20 μm thick Gd_2O_2S:Tb scintillator from Lexel Imaging System viewed with an Andor Neo sCMOS camera with 2560 × 2160 × 22 μm square pixels and 210 s acquisition time per projection (seven 30 s images with a median z-filter). The sample-to-scintillator distance was 2.0 cm giving a geometric blur of 33 μm.

3.4. Overview of five dynamic tomography runs

Five tomography runs were performed as the sample absorbed H_2 released from the 2.40 L reservoir. Each run began with evacuation of the gas manifold and sample with the turbomolecular pump to below 0.1 kPa, and then waiting until sample temperature stabilized at about 25 °C. The pressure logger and tomography data acquisition programs were started and acquisition of neutron images verified. Then, a valve on the gas manifold outside the beamline hutch was slowly opened. The H_2 pressure at the sample would rise to near that of the reservoir, then slowly fall to an equilibrium pressure, as listed in Fig. 4. Run #2 with 3613 projections, took 10.8 h. The hydrogen absorption process is exothermic; the sample temperature at the beginning of run #2 was 25.4 °C, increased to 32.5 °C at 10 min into the run, and then decreased to 24.2 °C at the end of the run. The equilibrium pressure data was converted to equilibrium H_2 saturation, based on the 113 g of $LaNi_5$ in the sample, and is plotted in Fig. 4.

The double-headed arrows in Fig. 4 denote the post-acquisition time windows selected for tomography reconstruction. The longer arrows encompass 100 projections and the shorter arrows correspond to 50 projections; the first 500 rotation stage angles are as shown in Fig. 1B, C. The right-most arrow denotes projection number 501 to the end of the tomography run, projections that are used to generate a steady-state view of the hydrogenation for that equilibrium hydrogen pressure.

3.5. Tomography reconstruction with MuhRec

Preliminary tomography reconstructions were performed with Faridani's Matlab algorithm [15] recoded into Mathematica and using the weighting scheme described in Eqs. (3)–(5). However, the Mathematica code is slow; a much faster reconstruction code is available with the new MuhRec package [7,16]. The FITS images from the NIST detector were flat-field corrected, then converted into absorption images in FITS format with filenames coded in terms of acquisition sequence, rotation angle, elapsed time, and H_2 pressure, along with a list of absorption images and corresponding rotation angles to be used for a tomography reconstruction. As shown in Fig. 4, reconstructions used 50, 100, or a large number of projections; 50 projections corresponds to a time window of about 530 s and twice that time for 100 projections. A rotation axis centering error, on the order of several pixels, was corrected in MuhRec. In this manner, each tomography run was reconstructed into six or eleven sequential 3D images of the hydrogen absorption process, with timings as shown in Fig. 4.

The hydrogenation of $LaNi_5$ to form $LaNi_5H_6$ is a perfect system for dynamic neutron tomography: The volume change is very large, about 25% based on unit cell volumes [17,18]. And, the predicted neutron scattering cross sections for thermal neutrons, based on published cross sections for elements and isotopes [3], are dramatically different; $LaNi_5$ and $LaNi_5H_6$ have $1/e$ path lengths of 6.9 and 1.4 mm, respectively. Visualizing dynamic processes in 3D plus time provides a unique perspective of a complex process. However, the challenge we face is maximizing time resolution, about 530 or 1060 s, at the cost of signal-to-noise ratio in the 3D image, 50 or 100 projections per data set.

3.6. Image processing

The primary visualization tool was Avizo 6 and 7 (VSG, Inc., Burlington, MA, USA), supplemented with ImageJ (NIH) and Mathematica (Wolfram).

Based on the active sample portion for hydrogenation, as shown in Fig. 3b, a subvolume of dimensions $474 \times 474 \times 500$ with 127 μm cubic voxels was selected for image analysis. A check of the voxel values for both the air surrounding the sample and the aluminum mounting bar showed consistent mean values across all reconstructed data sets. The dynamic tomography volumes were resampled to a courser resolution and a Gaussian filter was applied.

4. Results and discussion

4.1. Static, high resolution tomography

The four-tube sample holder was prepared with sieved grains and some alumina spacers. 2D neutron radiography was performed as H_2 was added and removed, leading to the selection of one sample tube for high resolution tomography. The selected tube, containing $\geqslant 1$ mm grains, was recentered on the rotation stage to reduce offset from the rotation axis. The sample was charged with H_2 to 0.4 MPa. The Andor Neo sCMOS camera with $2560 \times 2160 \times 22$ μm square pixels was used with the fixed angle acquisition sequence, Eq. (1).

At 0.4 MPa, many of the $LaNi_5$ grains contain some H_2 as can be seen by cracking in grains shown in Fig. 5. In Fig. 5, the blue spheres are spacers of Al_2O_3 added to the sample tube in order to accommodate volume expansion upon hydrogenation. The sample mass between spacers is 1 g, corresponding to roughly 10–20 grains of $LaNi_5$ (sieved, particle size $\geqslant 1.19$ mm) in the initial sample preparation. $LaNi_5$ grains do tend to fracture with repeated H_2 absorption, thus, the alumina spacers were added during sample preparation to help demarcate the initial grain loadings. Upon visual inspection (Avizo aided) comparison of grains in Fig. 5 with the 2D neutron radiography does lead to plausible identification of grains that are first to absorb H_2.

The 2D radiography shows the performance of $LaNi_5$ from 0 MPa to 0.54 MPa H_2 over 1.6 h and slowly back to 0 MPa. Three movie frames from the H_2 absorption run are shown in Fig. 6. The text over each image gives the image sequence number, elapsed time, and H_2 pressure. The objective of identifying the most reactive grains is difficult with 2D radiography because of overlapping grains in the 2D images, hence the need for dynamic tomography using the Greek Golden ratio angle acquisition sequence.

4.2. Dynamic tomography

In five sequential runs, a sample of $LaNi_5$ was exposed to H_2 and imaged in 3D during absorption with the Greek Golden ratio angle acquisition sequence of Eq. (2), as modified with the sort process shown in Fig. 1. The high neutron scattering cross Section (82.02 barn total bound scattering cross section) of ^1H provides the image contrast. Each data set covers more than 15,000 s of 3D observation, and the first 10,840 s of observations were analyzed in two parallel procedures (Figs. 1 and 4): (a) divided into five time windows, or, (b) divided into ten time windows. The sample consisted of 113 g $LaNi_5$ (not sieved) loaded into four tubes and activated with two cycles of [evacuate, heat, cool, hydrogenation]. Roughly 1/4 of the sample was successfully activated and the forthcoming

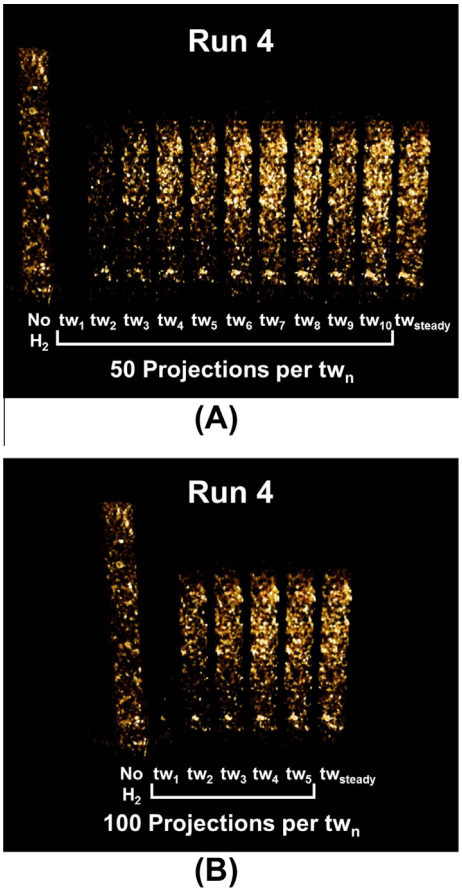

Fig. 7. Run #4 with $P_{eq} = 0.336$ MPa and 17.8% H_2 saturation (calculated for the entire 113 g $LaNi_5$ sample). For Figs. 7 and 8, each tw_n is the complete tomogram of the text object.

image analysis will be of the lower portion of one of the activated sample tubes as shown in Fig. 3b. Unlike the high resolution tomography of Fig. 5 which is based on a single sample tube in the tomography experiment, the dynamic tomography experiment imaged all four sample tubes; in the image analysis, we crop the reconstructed volume to show only one sample tube. The values of H_2 percent saturation refer to the potential hydrogen loading of the entire 113 g $LaNi_5$ contained in all four sample tubes; during dynamic tomography, all four tubes were opened to the hydrogen manifold.

Fig. 7 shows two data processing options for an experiment with slow addition of H_2 to an equilibrium pressure of 0.336 MPa. Similarly, Fig. 8 is also a H_2 absorption run to an equilibrium pressure of 0.248 MPa. On the left side of each figure, noted as 'No H_2, is a repeated display of the sample imaged at 0 MPa H_2, but shown with a lower threshold value for the volume rendering (Avizo voltex).

Each column of Figs. 7 and 8 represents a time window of ≈500 s for the 50 projection time windows and ≈1000 s for the 100 projection time windows. The consistent detection of particular $LaNi_5H_x$ grains or groups of grains from one time window to the next time window supports the premise that real objects are being detected.

Careful inspection of the figures, and of movies generated from these Avizo Voltex representations, shows some evidence of a "winking in and out" of view as, we suspect, a hydrogen-rich grain or group of grains is nicely defined by the projection rays in one time window, but less well defined by projections rays in the next time window. We judge this to be a minor problem for visual analysis, but could be problematic in a numerical analysis.

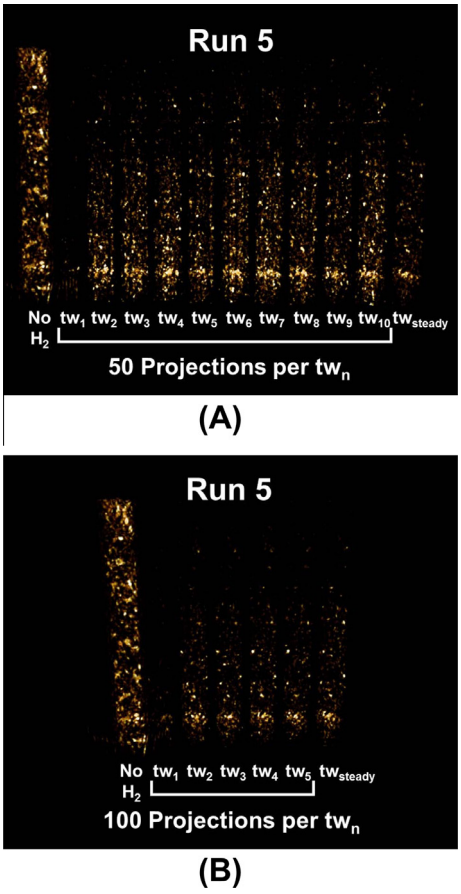

Fig. 8. Run #5 with P_{eq} = 0.248 MPa and 3.1% H_2 saturation (calculated for the entire 113 g $LaNi_5$ sample).

5. Conclusions

Neutron imaging beamtime is extremely precious, hence the need for experimental procedures that maximize the acquisition raw data and then allow flexibility in post-acquisition data processing. The Greek Golden ratio aids the study of a process slow with respect to the required for a single projection, but faster than a fully-sampled tomography run. The angle sequence calculation is trivial, however, it can be helpful to label projection data with both a sequence number and angle as the projections are reordered to generate a sinogram. The weighing scheme for each projection during the reconstruction is given by Eqs. (3)–(5).

The lengths of the sorted lists used in Figs. 1 and 2 were fixed at multiples of ten for procedure development. It is likely that improved performance would be found with lists lengths set to Fibonacci numbers, such as 55, 89 and 144.

The materials science question in this project is whether or not all grains of $LaNi_5$ exhibit equal reactivity with hydrogen. The tomography results shown in Figs. 7 and 8 are suggestive of a distribution of grain reactivity. The materials science question is better addressed by switching from $LaNi_5$ to $LaNi_{4.78}Sn_{0.22}$ [5]. The volume expansion in the Sn-doped sample is lower, hence leading to less cracking upon hydrogenation. This will likely lead to longer time scales for morphological changes and improve spatial resolution after reconstruction using dynamic tomography. A problem encountered with $LaNi_5$ is a tendency of large grains to fracture under the volumetric strain of hydrogen absorption. The use of alumina spacers and measured grain count and grain mass between spacers was very helpful during the matchup of tomographic reconstructions with 2D radiography of the hydrogen absorption/de-sorption process. The ideal wrap-up experiment is then slow hydrogen addition/evacuation with dynamic tomography.

The need to examine 3D morphology tomograms for samples which are changing *in situ* is addressed using a newly developed quasi-dynamic tomography scheme. Here, we illustrate the scheme for the hydrogenation of $LaNi_5$ to $LaNi_5H_6$ at various final H_2 gas pressure. This hydrogen absorption system is ideal because the large volume expansion, $\Delta V = 25\%$, and difference in neutron attenuation between the metal and hydrogenated metal states causes marked changes in the sample morphology and neutron beam attenuation. We investigate the time windows needed for reaction characterization in quasi-dynamic tomography as well as the number of projections.

For the run ending with 17.8% H_2 saturation (P_{eq} = 0.336 MPa), the grain hydrogenate as indicated by their volume change and increase in brightness. For this H_2 saturation, the first time window, at 50 projections per time window, to yield a full tomogram showing an granular structure nearly the same as the final state is tw_6. For the run ending at 3.1% H_2 saturation (P_{eq} = 0.248 MPa), slow hydrogen exchange between particles may account for the lack of a definitive final state image.

Acknowledgments

The NIST authors acknowledge support from the U.S. Department of Commerce, the NIST Radiation Physics Division, the Director's office of NIST, the NIST Center for Neutron Research, and the Department of Energy through interagency agreement No. DE-AI01–01EE50660. L.G.B. and T.A.D. gratefully acknowledge the support of materials science tomography from the National Science Foundation (CHE-0910937) and the NSF EPSCoR Cooperative Agreement No. EPS-1003897 with additional support from the Louisiana Board of Regents. A.F. also acknowledges NSF support (DMS-0709495). L.G.B. sincerely thanks Dr. Robert Bowman (JPL) for late night advice on sample activation and Eli Baltic (NIST) for

tremendous assistance with the H_2 gas manifold as well as careful attention to the safety issues. P.L. and J.J.V. acknowledge support from the Center on Nanostructuring for Efficient Energy Conversion (CNEEC) at Stanford University, an Energy Frontier Research Center funded by the U.S. Department of Energy, Office of Science, Office of Basic Energy Sciences under Award Number DE-SC0001060.

References

[1] P. Brookman, M. Braun, C. Keller, R. Solnit, A. Grundberg, Helios: Eadweard Muybridge in a Time of Change, Steidl, 2010.
[2] V. Sears, Neutron scattering lengths and cross sections, Neutron News 3 (3) (1992) 26–37.
[3] NIST, Neutron scattering lengths and cross sections. Available from: <http://www.ncnr.nist.gov/resources/n-lengths/>, (accessed August 17, 2011).
[4] H. Sakaguchi, Y. Satake, K. Hatakeyama, S. Fujine, K. Yoneda, M. Matsubayashi, T. Esaka, Analysis of hydrogen distribution in hydrogen storage alloy using neutron radiography, J. Alloys Compd. 354 (1–2) (2003) 208–215.
[5] D.L. Jacobson, D.S. Hussey, E. Baltic, T.J. Udovic, J.J. Rush, R.C. Bowman Jr., Neutron imaging studies of metal-hydride storage beds, Int. J. Hydrogen Energy 35 (23) (2010) 12837–12845.
[6] PlanckCollaboration, Planck Early Results: The thermal performance of Planck, Instrumentation and Methods for Astrophysics (astro-ph.IM), 2011. arXiv:1101.2023v1.
[7] A. Kaestner, P. Trtik, B. Muench, L. Butler, Spatio-temporal computed tomography of dynamic processes, SPIE Opt. Eng. 50 (2011) 123201.
[8] L. Butler, B. Schillinger, K. Ham, T. Dobbins, P. Liu, J. Vajo, Neutron imaging of a commercial Li-ion battery during discharge: application of monochromatic imaging and polychromatic dynamic tomography, Nucl. Instr. Meth. A 651 (1) (2011) 320–328.
[9] F. Natterer, F. Wübbeling, Mathematical Methods in Image Reconstruction, SIAM, Philadelphia, PA, 2001.
[10] T. Köhler, A projection access scheme for iterative reconstruction based on the golden section, Nuclear Science Symposium Conference Record, 2004 IEEE 6 (2004) 3961–3965.
[11] Wolfram, Golden Ratio. Available from: <http://mathworld.wolfram.com/GoldenRatio.html> (accessed August 17, 2011).
[12] I. Kazantsev, S. Matej, R. Lewitt, Optimal ordering of projections using permutation matrices and angles between projection subspaces, Electron. Notes Discrete Math. 20 (2005) 205–216.
[13] A. Katsevich, An accurate approximate algorithm for motion compensation in two-dimensional tomography, Inverse Prob. 26 (6) (2010) 065007.
[14] U. Birk, M. Rieckher, N. Konstantinides, A. Darrell, A. Sarasa-Renedo, H. Meyer, N. Tavernarakis, J. Ripoll, Correction for specimen movement and rotation errors for in-vivo optical projection tomography, Biomed. Opt. Express 1 (1) (2010) 87–96.
[15] A. Faridani, Introduction to the Mathematics of Computed Tomography, vol. 47, MSRI Publications, Cambridge University Press, 2003, pp. 1–46.
[16] A. Kaestner, MuhRec—a new tomography reconstructor, Nucl. Instr. Meth. A 651 (1) (2011) 156–160.
[17] E. Kisi, C. Buckley, E. Gray, The hydrogen activation of LaNi5, J. Alloys Compd. 185 (2) (1992) 369–384.
[18] V. Burnasheva, V. Iartys, N. Fadeeva, S. Soloviev, K. Semenenko, Crystal structure of LaNi5D6, Doklady Akademii Nauk Sssr 238 (4) (1978) 844–847.